Hydrodynamics and filtering of knotted ring polymers in nanochannels

Lisa B. Weiss,[*,†] Mattia Marenda,[‡,¶] Cristian Micheletti,[‡] and Christos N. Likos[†]

†*Faculty of Physics, University of Vienna, Boltzmanngasse 5, A-1090 Vienna, Austria*

‡*SISSA, International School of Advanced Studies, via Bonomea 265, I-34136 Trieste, Italy*

¶*MRC Institute of Genetics and Molecular Medicine, University of Edinburgh, Crewe Road, Edinburgh EH4 2XU, United Kingdom*

E-mail: lisa.weiss@univie.ac.at

Abstract

We study the hydrodynamic transport of knotted ring polymers through modulated channels, establishing that the transport velocity is strongly dependent on the ring topology for Peclet numbers smaller than unity. As soon as convection dominates, transport properties become insensitive to the presence and type of knots. We identify two distinct modes of transport, corresponding to the motion being led by the knotted or unknotted portions of the ring, most surprisingly without impact on separation efficiency. The modes can be selected by the channel geometry and this could be harnessed to design nanofluidic devices for the continuous topological sorting of entangled biopolymers.

1 Introduction

Channel confinement is increasingly used as the method of choice for examining the impact of topology on the physical behavior of polymers. In recent breakthrough experiments, linear

1

DNA filaments were trapped inside a channel and their metric properties were monitored, while their knotted state was changed by compression or elongation.[1–3] The measurements, together with models and simulations, helped establish how the knotting and unknotting kinetics is coupled to the global dynamics of the chain,[1–5] how knot size fluctuates in and out-of-equilibrium,[6–8] and how the motion of knots along the confined chains responds to an externally-imposed flow or elongational field.[2,3] Besides the relevance to polymer physics, these aspects have bearings in applicative contexts such as genomic barcoding, where erroneous readouts can be caused by the backfolded contour of knotted DNA.[9] Channel confinement has been applied to ring polymers as well. These systems have been mostly studied for their static properties, and particularly for the non-monotonic dependence of knotting probability on channel width,[6,8] which has been associated to the free energy balance between the knotted and unknotted portions.[6,10]

By contrast, the rich kinetic behavior of confined knotted rings is still underexplored and basic properties, such as transport, have remained unclarified. In this work, we examine the unique mobility properties resulting from the combined action of hydrodynamic flow and channel geometry. We use hydrodynamic simulations to study how differently-knotted rings flow through channels with a periodic hourglass topography, where chambers, which entropically trap the polymers, and narrowings, which hinder knot passage, appear in alternation. This, as we show, realizes a minimalistic system where the diffusive and convective transport components of different knot types can be competitively adjusted via the flow strength or channel geometry. It also allows us to test the hypothesis of[11] that channel shape can be optimized to make possible the separation of rings with same length but different knot types, as needed, e.g., for topological profiling of viral DNA. Up to now, filtering mechanisms for chains and rings have been proposed,[12,13] which however are not aimed at discriminating rings by knot type. We demonstrate that the mobility of the rings depends strongly on topology for Peclet numbers smaller than unity. We further establish that transport can occur in two modes, one which is led by the knotted portion of the polymer, the other one

2

described by the knotted section trailing behind. These two modes do not affect separation efficiency and are owed to the interplay of constriction radius, knot size and hydrodynamic backflow. The results provide quantitative criteria and insights that we expect will be useful for designing nanofluidic devices for topological sorting of entangled polymers.

The rest of the manuscript is organized as follows. We introduce the polymer model, the hydrodynamic simulation technique and the system set-up in section 2. Subsequently, we present equilibrium properties of polymers in section 3 and their convective transport in such corrugated channels in section 4. In section 5, a detailed analysis of knot conformations and modes of translocations is presented, in section 6 we summarize and draw our conclusion.

2 Model and simulation details

We employed a bead-spring model, suitable for flexible ring polymers in a good solvent, consisting of $M = 150$ monomers. Excluded-volume interactions between monomer i and j were modeled via the shifted and truncated Weeks-Chandler-Andersen(WCA) potential U_{WCA}:[14]

$$
U_{\mathrm{WCA}} = \frac{1}{2} \sum_{i=1}^{M} \sum_{i \neq j=1}^{M} 4\varepsilon_{\mathrm{MM}}
$$
$$
\left[\left(\frac{\sigma_{\mathrm{MM}}}{r_{i,j}} \right)^{12} - \left(\frac{\sigma_{\mathrm{MM}}}{r_{i,j}} \right)^{6} + \frac{1}{4} \right] \Theta(2^{1/6}\sigma_{\mathrm{MM}} - r_{i,j}). \tag{1}
$$

Here, $\varepsilon_{\mathrm{MM}}/k_{\mathrm{B}}T = 1$ is the bead-bead interaction strength, $k_{\mathrm{B}}T$ the thermal energy, σ_{MM} denotes the bead diameter, $r_{i,j}$ the distance between beads i and j, and $\Theta(\cdots)$ is the Heaviside function.

Polymeric bonds between subsequent monomers were accounted for by the finite extensible nonlinear elastic (FENE)-potential U_{FENE}:[15]

$$U_{\text{FENE}} = \begin{cases} \sum_{i=1}^{M} \frac{k}{2} R_0^2 \ln\left[1 - \left(\frac{r_{i,i+1}}{R_0}\right)^2\right] & \text{if } r_{i,i+1} \leq R_0, \\ \infty & \text{otherwise,} \end{cases} \tag{2}$$

with the standard Kremer-Grest parameters for the bond constant $k = 30\,\varepsilon_{\text{MM}}/\sigma_{\text{MM}}^2$ and the maximum bond extension $R_0 = 1.5\sigma_{\text{MM}}$.[16] Note that in Eq. (2), if $i = M$, then $i + 1 \hat{=} 1$, to ensure a closed loop. The interplay of the FENE connectivity term and the excluded volume interaction ensures that the initial topology of the rings is maintained at all times. For the latter we consider the three simplest types of knots, namely: the unknot (0_1), the trefoil (3_1) and the figure-of-eight (4_1) knot, see Fig. 1(a).

The metric properties of the rings were mostly characterized by employing suitable combinations of the elements of the gyration tensor $\hat{\mathbf{G}}$:[17]

$$\hat{G}_{\alpha\beta} = \frac{1}{M} \sum_{i=1}^{M} s_{i,\alpha} s_{i,\beta}. \tag{3}$$

Here, α, β are the Cartesian components of the bead position, $\mathbf{s}_i$, relative to the polymer's center of mass (CoM). The gyration radius $\hat{R}_g$ is expressed as:

$$\hat{R}_g = \sqrt{\text{tr}(\hat{\mathbf{G}})}. \tag{4}$$

Here, the hat superscript indicates instantaneous values, while no such superscript is used for time-averaged values. In addition to the gyration radius, we also computed the longitudinal span, S. The span provides a measure of the footprint of the ring projected along the channel axis, which is parallel to the x Cartesian axis, with r_i being the position of bead i:

$$S = \max_i(r_{i,x}) - \min_i(r_{i,x}) . \tag{5}$$
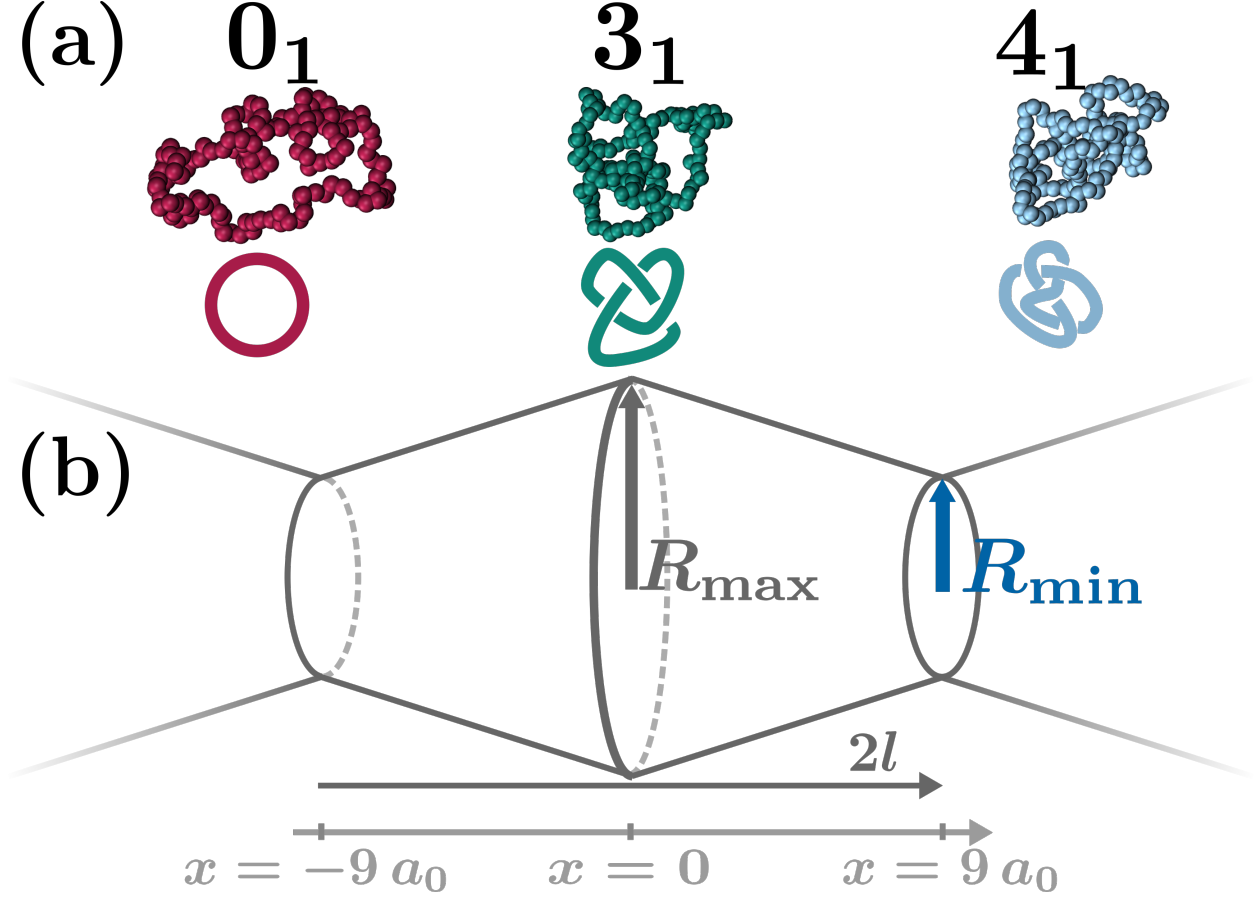
4

Figure 1: (a) Typical conformations of circular polymers of $N = 150$ beads of diameter $a_0 = \sigma_{MM}$ and tied with 0_1, 3_1 and 4_1 topologies. (b) Sketch of a single unit, of which the channel is constructed by periodic repetition. The radius of the largest circular section is R_{max} and that of the constriction is R_{min}.

To identify the knotted region we used the method of Refs.,[18,19] as implemented in the KymoKnot software package.[20] The algorithm identifies the smallest portion of the ring that, after a suitable closure, has the same topology of the entire ring. Tracking this portion during the simulation provides the instantaneous values of knot features, such as the knot contour length, ℓ_K, and the position of its center of mass, KCoM. By restricting the sum in Eq. (3) to the monomers of the knotted subpart of the ring, we calculated the radius of gyration of the knotted region $R_{g,K}$ via Eq. (4).

The importance of convective versus diffusive polymer transport is captured by the dimensionless Peclet number,

$$Pe = \frac{v_P R_{\mathrm{g}}}{D_{\mathrm{P}}} \ .$$ (6)

In Eq. (6), v_{P} is the average transport velocity of each polymer topology and R_{g} and D_{P} are the average gyration radius and diffusion coefficient in bulk, respectively. Thus, Pe changes with polymer topology at constant flow strength and for $Pe < 1$, a polymer diffuses faster over its characteristic length scale R_g than being transported convectively over the same distance.

The general setup considered in this study is illustrated in Fig. 1(b). The system consists of a cylindrical channel with a periodic hourglass modulation, obtained from the mirror juxtaposition of truncated cones. Its geometry is specified by the large and small diameters, $2R_{\mathrm{max}}$ and $2R_{\mathrm{min}}$ respectively, and by the longitudinal extension of the repeated modular chamber, $2l$. The values of R_{max} and l are both set equal to $9a_0$, with $a_0 = \sigma_{\mathrm{MM}}$, so to be larger but comparable to the average gyration radius of unknotted rings in bulk, $R_{\mathrm{g}} \simeq 6.99 \pm 0.08\,a_0$ for the considered chain length. The ratio of polymer volume to chamber volume has been evaluated as optimal sorting conditions [11,21] and is the same as for a chain of $M = 300$ in the setup of Ref. [11] Previously, such entropic traps combined with electric fields were used to separate dsDNA by its size, but not topology. [22] The WCA potential defined in Eq. (1) is employed for the excluded volume interaction between monomers and the channel wall; in this case $r_{i,j}$ denotes the distance between monomer i and the closest point at the channel wall, j. When beads are close to the narrowing, a normal vector to the wall cannot be defined, thus the length of the shortest vector, which connects the monomer and the constriction, is chosen as distance.

To include solvent mediated monomer-monomer and monomer-wall hydrodynamic interactions, we employed the Multi-Particle Collision (MPC) fluid model. [23,24] This particle-based approach offers the advantage of conserving locally mass, energy and momentum, thus fulfilling the Navier-Stokes equations while also accounting for thermal fluctuations. As there

is no potential acting between MPC fluid particles, fluid particles and walls, as well as fluid particles and monomers, the MPC approach is computationally much less onerous than Molecular Dynamics (MD) simulations with explicit solvent and it allows to bridge the time scales associated with the solvent and solute.[25] Furthermore, many fluid properties, such as transport coefficients can be calculated analytically.[26,27]

The algorithm evolves in two steps; firstly, particles are propagated ballistically during the streaming step over a time interval h:

$$\mathbf{x}_i(t+h) = \mathbf{x}_i(t) + h\mathbf{v}_i(t) \tag{7}$$

with $\mathbf{x}_i(t)$ and $\mathbf{v}_i(t)$ representing particle's i position and velocity at time t, respectively. Secondly, momentum between solvent particles is transferred in the collision step. Here, particles are assigned to cells of length a_0, and then the particles' velocities relative to the center of mass velocity $\mathbf{v}_{\text{cell,COM}}$ of a cell are rotated by a fixed angle α around a randomly oriented axis via the rotation operator $\mathbf{\Omega}_\alpha$:[26]

$$\mathbf{v}_i(t+h) = \mathbf{v}_{\text{cell,COM}}(t) + \mathbf{\Omega}_\alpha \left[\mathbf{v}_i(t) - \mathbf{v}_{\text{cell,COM}}(t)\right]. \tag{8}$$

Conveniently, the particles' mass m_{F}, the thermal energy $k_{\text{B}}T$ and the length of a cell a_0 are set equal to unity, thus defining the natural unit of time, $t_0 = a_0\sqrt{\frac{m_{\text{F}}}{k_{\text{B}}T}}$. The kinematic viscosity of the MPC-fluid, a measure of how fast momentum diffuses, is determined by the rotation angle $\alpha = 130°$, the collision time step $h = 0.1\,t_0$ and the average solvent number density $\rho = 5\,a_0^{-3}$, yielding a kinematic viscosity $\nu = 0.79a_0^2/t_0$ (dynamic viscosity of $\eta = m_{\text{F}}\nu\rho = 3.96\,m_{\text{F}}/(a_0t_0)$) for the chosen parameter set.[28,29] A random grid shift is performed before every collision step,[30] to restore Galilean invariance. Liquids are characterized by the dominance of collisional momentum transport compared to diffusive momentum transport, which is expressed by Schmidt numbers larger than unity.[25] In our simulations,

the Schmidt number $Sc = \nu/D_F = 12.4$ with $D_F \approx 0.064\,a_0^2 t_0^{-1}$ being the analytically calculated diffusion coefficient of fluid particles. Please note that at small collision time steps there is a discrepancy between analytical description and measured values due to a break down of the random chaos approximation.[31] As hydrodynamics are preserved down to a cell level,[32] the monomer size was set equal to the size of a collision cell, $\sigma_{MM} = a_0$.

To simulate buoyant beads, the mass of a polymer bead m_M is set equal to the average mass of a cell filled with solvent only ($m_M = \rho m_F a_0^3 = 5\,m_F$). During streaming of MPC-particles, monomers are propagated via MD with a time step $\delta = h/150$; this small time step ensures as well the conservation of topology. The coupling between the MD and MPC algorithm is accomplished by inclusion of monomers in the collision step.[33] To create a flow, a body force $f = m_F g$ with acceleration g is applied to all solvent particles, leading quickly to a steady state flow profile. The average fluid flow velocity is directly proportional to the applied flow velocity, see Fig. 2. In a geometry with longitudinally varying cross section, flow velocities must be as slow as to ensure that fluid particles can diffusively explore the cross section, which is ensured by the fluid Peclet number $Pe_F \ll 1$. In our simulations the maximum $Pe_F = 0.03$, taking as characteristic length a cell size a_0. Additionally, we verified that the fluid particle density resolved in radial and longitudinal directions is constant. Furthermore, our simulations result in Mach numbers $Ma \ll 1$, which is the ratio of flow velocity to sound velocity, and $Ma \ll 1$ is a characteristic of a fluid.[25] We employed bounce-back rules for solvent particles colliding with the walls to account for stick boundary conditions between fluid and wall, in addition to virtual particles.[34,35] At the midpoints $R(x) = R_{max}$ multiple reflections of fluid particles at the channel walls can occur, which are accounted for by placing fluid particles to the closest point at the wall and assigning them random velocities in normal and tangential direction to the channel wall, as used in the case of colloids.[36] We have adjusted the thickness of the virtual particle layer, such that the combined virtual particle / fluid particle distribution during the random grid shift reproduces a Poisson distribution with average number of particles ρa_0^3, and the distribution of relative
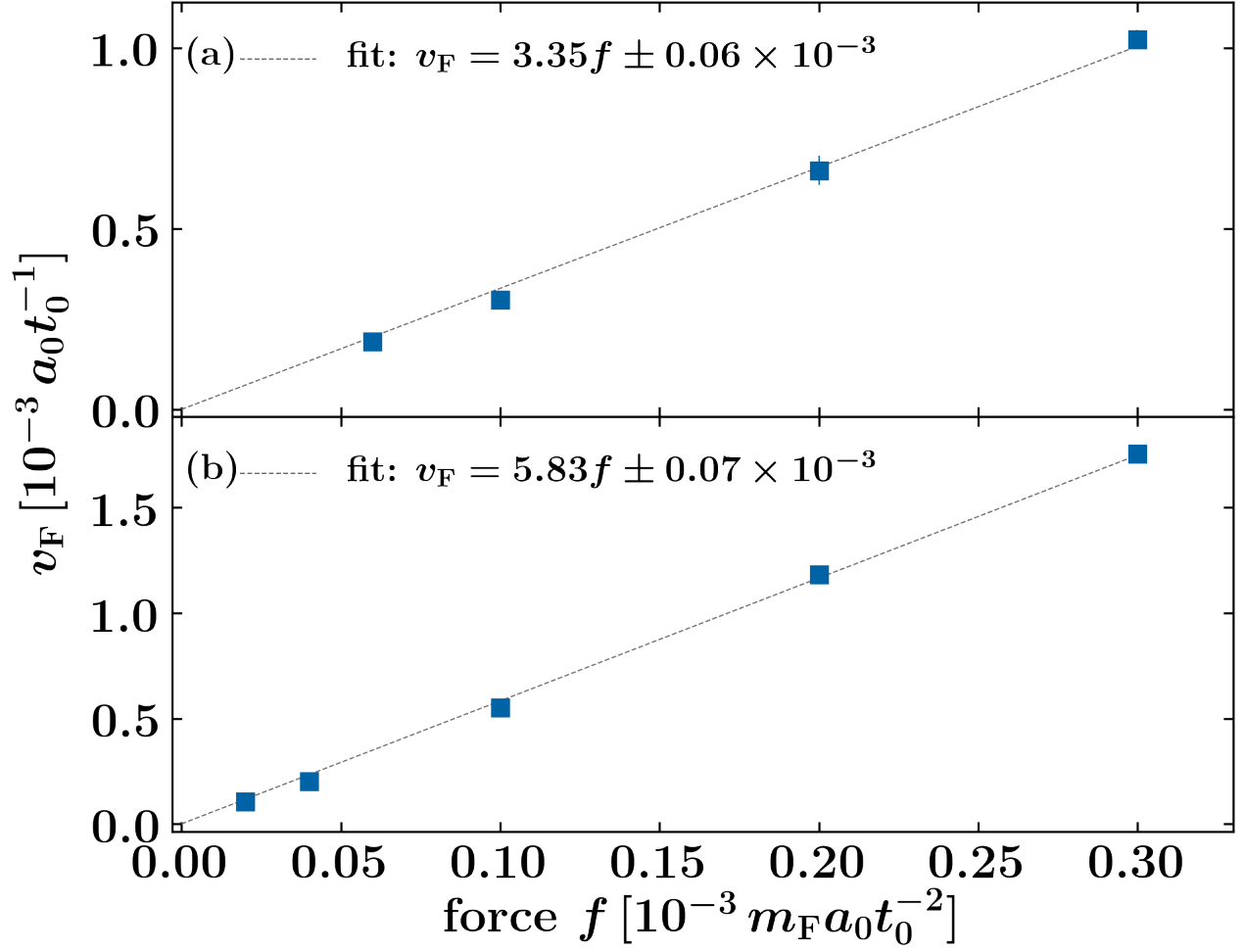
8

Figure 2: The proportionality of the average fluid flow velocity v_{F} to the body force f, which is applied to fluid particles only, is shown for a channel with a constriction of (a) $R_{\mathrm{min}} = 4\,a_0$ and (b) $R_{\mathrm{min}} = 5\,a_0$.

velocities of fluid and virtual particles, following a Maxwell-Boltzmann distribution. The latter is only fulfilled when employing the Maxwellian thermostat,[37] as we do.

Error bars are calculated from four simulations started from independent initial configurations. Error propagation is explicitly taken into account. Note that the 3_1 knot is chiral, thus we initialized an equal number of independent simulations with every enantiomer, although we do not expect any influence of chirality in this set-up.

3 Equilibrium properties in the bulk and in confinement

Bulk properties of ring polymers of $M = 150$ monomers bearing 0_1, 3_1 or 4_1 knots are summarized in Table 1, obtained by simulations in a cubic box of size $L = 50\,a_0$ with periodic boundary conditions. Table 1 indicates the radius of gyration R_g, diffusivity in bulk D_{bulk}, the longest relaxation time τ, which was calculated as the time it takes for a polymer to diffuse over its R_g and the polymer transport velocity at $Pe = 1$, $v_{Pe=1}$.

Table 1: Summary of the equilibrium properties as the radius of gyration R_g, diffusion coefficient D_{bulk}, characteristic time τ and polymers transport velocity at $Pe = 1$, $v_{Pe=1}$, of the investigated knots 0_1, 3_1 and 4_1. The data were obtained by simulating polymers in an unconfined MPC liquid.

knot	R_{g} $[a_0]$	D_{bulk} $[a_0^2 t_0^{-1}]$	τ $[t_0]$	$v_{Pe=1} [a_0 t_0^{-1}]$
0_1	6.99 ± 0.08	$(1.6 \pm 0.2) \times 10^{-3}$	5090	2.1×10^{-4}
3_1	6.11 ± 0.05	$(1.81 \pm 0.09) \times 10^{-3}$	3438	3.0×10^{-4}
4_1	5.30 ± 0.02	$(1.99 \pm 0.09) \times 10^{-3}$	2353	3.7×10^{-4}

R_g, a static quantity, is in good agreement with Langevin simulation of polymers without solvent,[11] whereas diffusivities, a dynamic quantity, are different. This is due to the fact that in Rouse-like dynamics the friction experienced by the polymer is $\zeta = M\zeta_M$ with ζ_M being the friction coefficient per monomer, thus distinct topologies have the same bulk diffusion coefficient.[17,38] Contrary, when hydrodynamic interactions are included, as in our case *via* the MPC solvent, friction is proportional to $\zeta \approx \pi\eta R_H$, with η being the viscosity of the solvent and R_H the hydrodynamic radius.[17,39] As R_H varies with topology, diffusivities in

bulk are distinct for 0_1, 3_1 and 4_1 knots, with the most complex (simplest) knot diffusing the fastest (slowest), as shown in the inset of Fig. 3. Thus, in bulk and dilute solution HI are of utmost importance.

Next, we investigated the equilibrium properties in confinement. To evaluate the optimal constriction radius R_{min}, the diffusivities in longitudinal direction D_x were measured at fixed $R_{\mathrm{max}} = 9\,a_0$ as a function R_{min} as shown in Fig. 3. All modulated channels consisted of four chambers, compare Fig. 1(b). In doing so, we prevented spurious self-interactions of polymers when applying periodic boundary conditions in axial direction. To measure diffusivities we followed closely the approach in Ref.[11] and determined diffusivities via mean squared displacements larger than the ones related to intra-chamber diffusion. In a channel of uniform radius $R_{\mathrm{min}} = R_{\mathrm{max}} = 9\,a_0$, the unknot diffuses slower than non-trivial topologies, similar to diffusion in bulk, although D_x is diminished. As R_{min} is gradually reduced, while keeping R_{max} constant, the diffusivity ranking is inverted, since the height of the entropic barrier during translocation depends on polymer topology. Large differences in D_x across the considered topologies are observed for $R_{\mathrm{min}} \in \{4, 5\}\,a_0$, and hence we focused our study on these constriction sizes. Please note that for the smallest considered constriction, $R_{\mathrm{min}} = 4\,a_0$, the knotted ring polymers very rarely diffused out of the chamber in the absence of an active flow, thus D_x could not be determined exactly. We derived an upper estimate for D_x for the 3_1 and 4_1 topology in a channel with narrowing $R_{\mathrm{min}} = 4\,a_0$ via $D_x \le (2l)^2/T = 5 \times 10^{-5} a_0^2 t_0^{-1}$. Here, $2l$ is the span of a single chamber and T is the total simulation length.

The differences in diffusion coefficient are promising indicators that topological separation could be achieved as long as the intrinsic stochasticity of the diffusive process is significantly suppressed. This can be achieved by using active flows, as we show below.
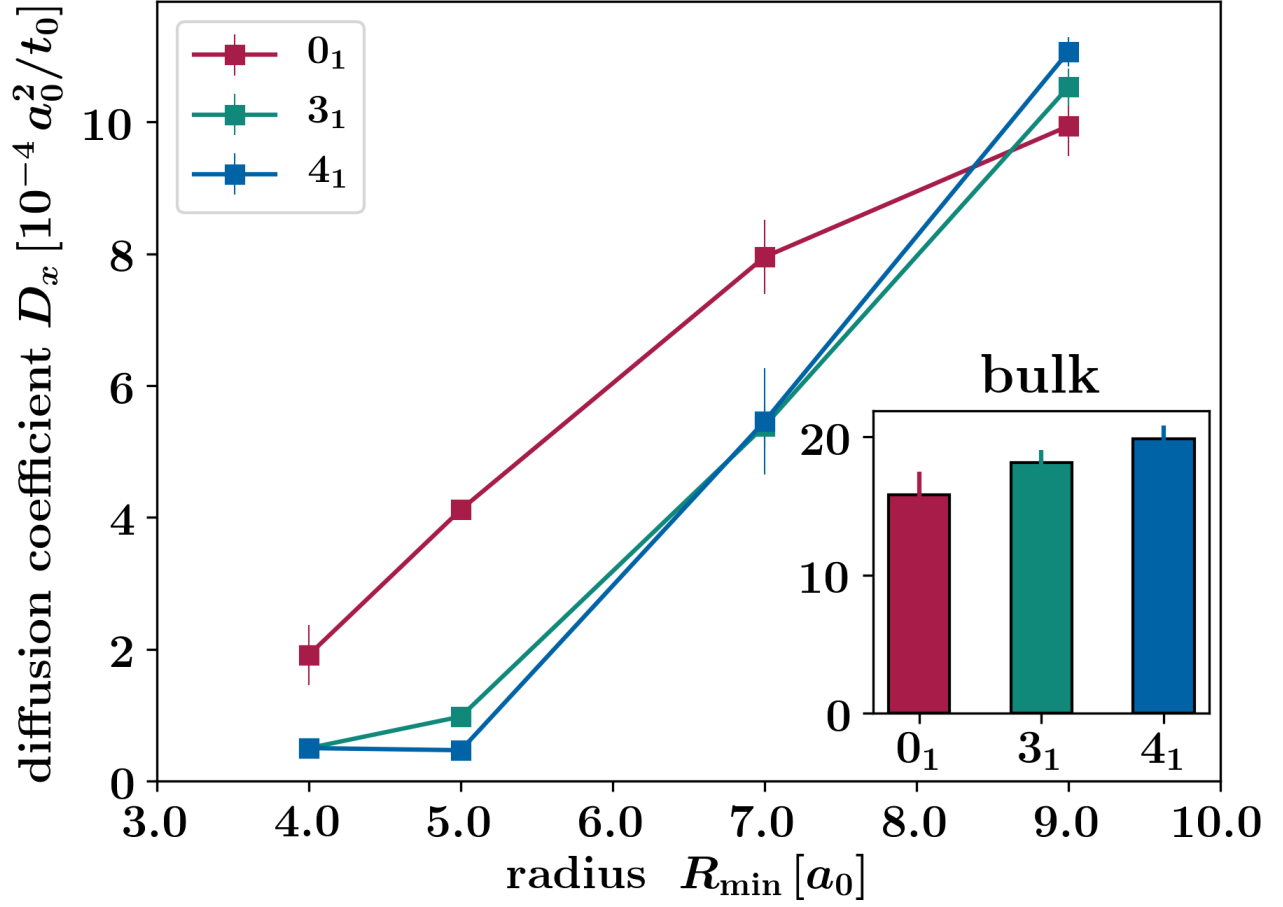
Figure 3: Diffusion coefficient in longitudinal direction D_x as function of the narrowing radius $R_{\min}$. In all setups $R_{\max} = 9\,a_0$. The inset shows the diffusion coefficient in bulk for all three topologies.
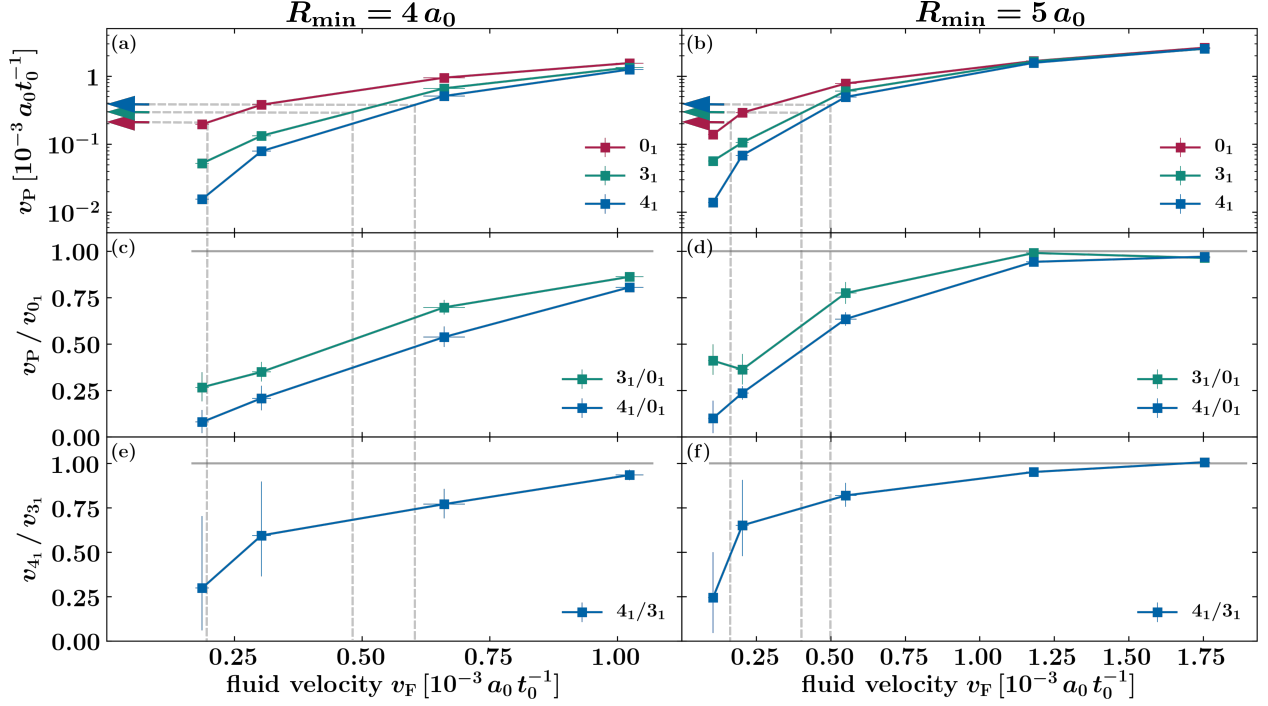
Figure 4: Average transport velocity of knotted rings, v_P, in units of $a_0\,t_0^{-1}$, are shown in (a)-(b), average polymer velocity v_P as a fraction of the transport velocity of the unknot v_{0_1} in (c)-(d), and the ratio of transport velocity of the figure-of-eight knot to the trefoil knot v_{4_1}/v_{3_1} in (e)-(f), in all plots as a function of the average fluid velocity v_F. (a),(c) and (e) are the results for a constriction radius of $R_\mathrm{min} = 4\,a_0$ and (b),(d) and (f) $R_\mathrm{min} = 5\,a_0$. Arrows show the polymer velocity at $Pe = 1$, $v_{Pe=1}$, dashed lines indicate the corresponding fluid velocity for every topology.

4 Convective transport in corrugated nanochannels

We characterize the resulting flow strength by the steady-state fluid flow velocity v_F, which is directly proportional to the applied force f, as shown in Fig. 2. Figs. 4(a) and 4(b) show the transport velocity v_P of all polymer topologies as a function of the fluid flow velocity v_F. At small fluid velocities v_P is distinct for distinct topologies, whereas as soon as $Pe > 1$ these differences fade. The polymer velocity is increasing monotonically with v_F, but not linearly, contrary v_F is a linear function of f. Table 2 summarizes the applied body force f, fluid velocity v_F, polymer velocity v_P and Peclet numbers Pe. Figs. 4(c) and 4(d) show the transport velocity of the 3_1 and 4_1 topologies with respect to the unknot as a function of fluid velocity v_F. When the Peclet number of the 3_1 or 4_1 is smaller than unity, the unknot is transported faster by up to one order of magnitude compared to knotted structures, enabling

a reliable separation of topologies for both constriction radii. Here, we take as criterion for reliable filtering at least a twofold difference in v_P.

Figure 4(e) and 4(f) show the relative transport velocity of the figure-of-eight knot to the trefoil knot v_{4_1}/v_{3_1}. For small flow strengths, we find as well a four-fold difference in the relative transport velocities, though bearing a large statistical uncertainty. Thus, we hypothesize that, besides discriminating between knotted and unknotted states, a separation of distinct knotted topologies could be achieved at low flow strengths.

Contrary to other separation techniques, our proposed setup allows for a separation of dilute mixture of distinct ring polymer topologies without any pre- or post-treatment. The species, for instance, must be separated by mechano-chemical means in gel electrophoresis, which additionally is restricted to charged polymers of relatively short length. Furthermore, these channels offer the possibility of an easy upscaling by arranging several of them in an array.

Table 2: Summary of the average fluid velocity v_F and Peclet number Pe of distinct topologies as a function of applied body force f used to create the flow. Grey shaded cells highlight Peclet numbers smaller than unity. Please note that not all values of the body force f were applied to every constriction radius.

$f\,[10^{-3}m_F a_0 t_0^{-2}]$	$R = 4\,a_0$				$R = 5\,a_0$			
	$v_F\,[10^{-3}\,a_0 t_0^{-1}]$	Peclet number Pe			$v_F\,[10^{-3}\,a_0 t_0^{-1}]$	Peclet number Pe		
		0_1	3_1	4_1		0_1	3_1	4_1
0.02					0.1049 ± 0.02	0.61	0.19	0.04
0.04					0.203 ± 0.02	1.28	0.35	0.18
0.06	0.187 ± 0.01	0.86	0.18	0.04				
0.10	0.303 ± 0.02	1.67	0.45	0.21	0.55 ± 0.04	3.42	2.02	1.31
0.20	0.661 ± 0.04	4.17	2.22	1.35	1.18 ± 0.03	7.33	5.54	4.17
0.30	1.02 ± 0.03	6.84	4.50	3.33	1.76 ± 0.02	11.51	8.47	6.75

For both radii, separation works *most efficiently* under the condition that Peclet numbers of all but one topology are smaller than unity. For higher Peclet numbers, polymers are prevented from exploring all degrees of freedom in radial direction. This effectively eliminates the free energy barrier across chambers, leading to a topology-independent transport.

Fig. 5 qualitatively shows how flow erodes the free energy barrier and equalizes the center of mass (CoM) distribution. For every topology, the axial and radial CoM position
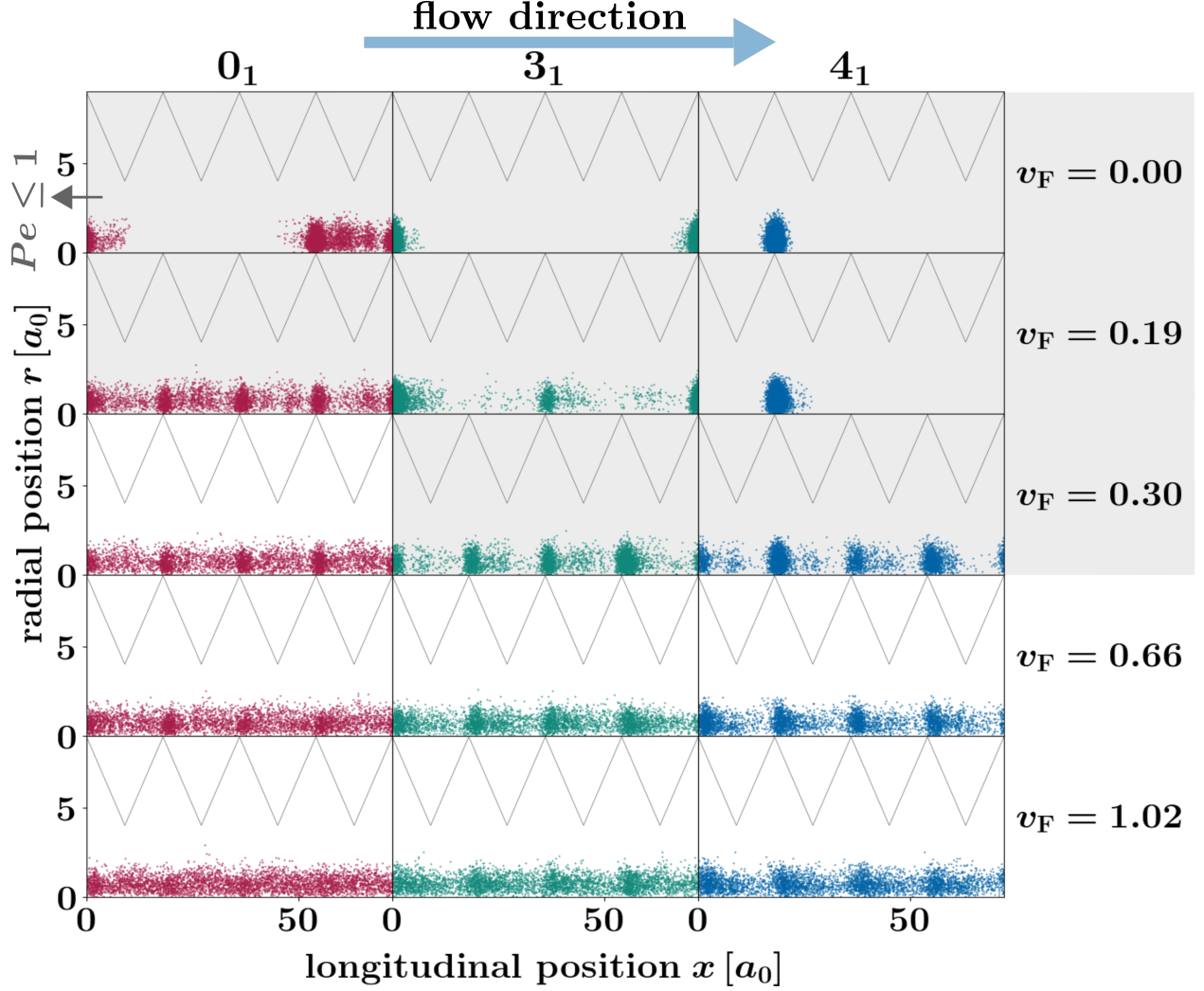
Figure 5: Radial and longitudinal CoM positions sampled at time intervals $\Delta = 500\,t_0$ over a time span of duration $t = 2.28 \times 10^6\,t_0$. Shown data are for all topologies and flow strengths in a channel of $R_{\mathrm{min}} = 4\,a_0$. Longitudinal periodic boundary conditions apply. Gray shaded regions correspond to $Pe \leq 1$. The upper row, $v_{\mathrm{F}} = 0$, is for the equilibrium (passive transport) case. v_{F} values are given in units of $10^{-3}a_0t_0^{-1}$.

are shown against the sketched outline of the channel. For $Pe < 1$ all topologies show a strong preference to be located at the midpoints of the chambers, where $R(x) = R_{\mathrm{max}}$. With increasing flow strength this preference is diminished, and CoM populates as well the position of the narrowing, indicating an enhanced mobility of every topology. Even though for $Pe > 1$ the CoM is more frequently located at the constrictions compared to smaller Peclet numbers, the 3_1 and 4_1 topologies are still likely to have their CoM at the midpoints, explaining even at $Pe > 1$ a distinct transport velocity in Fig. 4(c).

Flow does not only influence the CoM position distribution, but shows as well a strong
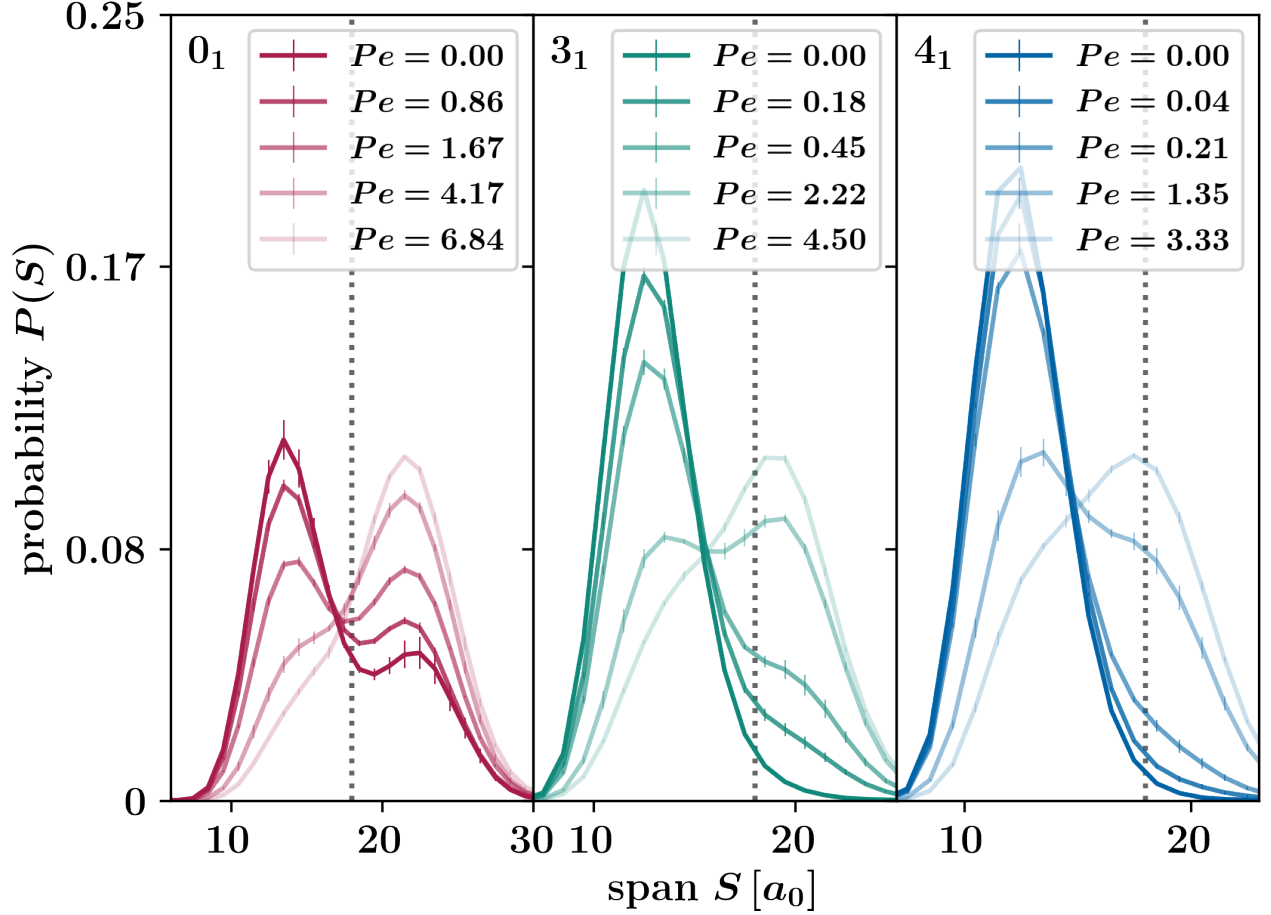
Figure 6: Probability distributions of the longitudinal span, $P(S)$, for polymers of different topologies for constriction radius $R_{\min} = 4\,a_0$. Lighter colors are used for increasing Peclet numbers.

influence on single molecule conformations. The shape of macromolecules, as for example the span S, see Eq. (5), reacts highly sensitively to Peclet numbers as well. Fig. 6 shows the probability that the rings have a certain longitudinal span, S, for various flow strengths and $R_{\min} = 4\,a_0$. When $Pe < 1$, the probability distribution $P(S)$ is similar to the equilibrium (passive transport) case, $Pe = 0$. The unknot has for this regime a noticeably larger probability to span a distance larger than the length of a single chamber, which is indicated by a vertical dotted line, explaining its higher diffusivity in equilibrium in modulated channels. As soon as $Pe > 1$ polymers show a strong deviation from the $Pe = 0$ case.

The enhanced elongation in longitudinal direction is accompanied by a radial contraction, which facilitates translocation into new chambers. This explains on a microscopic basis, why the difference in average transport velocity diminishes at high flow strengths. Here, we
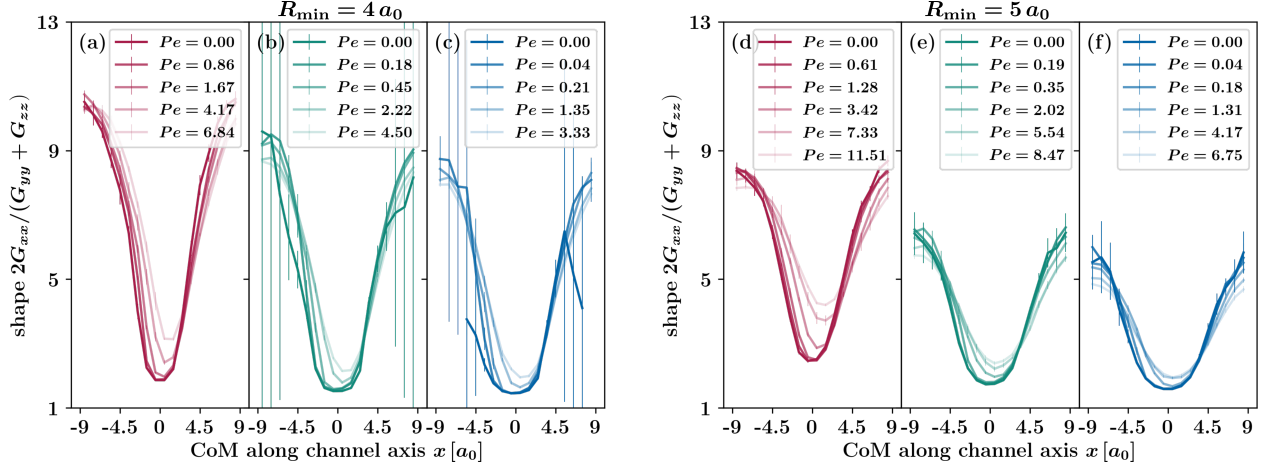
16

Figure 7: Shape of a polymer as a function of its CoM position along a chamber. (a)-(c) depict a narrowing of $R_{\min} = 4\,a_0$, whereas (d)-(f) correspond to $R_{\min} = 5\,a_0$. The unknot is depicted in red, the trefoil knot in green and the figure-of-eight knot in blue. With lightening color the flow strength increases.

evaluated the shape of polymers based on the time averaged elements of the trace of the gyration tensor $2G_{xx}/(G_{yy} + G_{zz})$ as shown in Figs. 7(a)-7(c) for $R_{\min} = 4\,a_0$ and 7(d)-7(f) for $R_{\min} = 5\,a_0$ as a function of the CoM position along the channel axis x, projected into a single chamber. For polymers in equilibrium and bulk this parameter is unity; as soon as it starts stretching out longitudinally due to confinement or flow in axial (x) direction, it exceeds unity. A common feature in Figs. 7(a)-7(f) is that at $x = 0$ the polymer is the closest to being point-symmetrically distributed in space on average, whereas at the position of the constriction, the polymer is most elongated along the channel axis. Furthermore, increasingly strong flows result in a stronger shape deformation at $x = 0$, i.e., $2G_{xx}/(G_{yy} + G_{zz}) > 1$, and less deformation at the narrowing $|x| = 9\,a_0$. Taking these two effects together, polymers show at high fluid flow velocities less changes in their shape across the chamber, compared to equilibrium. One can ascribe this to the lack of time to fully relax back to the equilibrium shape. Comparing distinct topologies, it is evident that the unknot can deform much more along a chamber, compared to knotted structures, which are hindered to do so by their essential crossings, see Figs. 7(a) and 7(b)/7(c) [7(d) and 7(e)/7(f)]. When investigating the impact of the narrowing on the shape deformation, we must distinguish two cases; when the CoM is located at $x = 0$, the polymer is less deformed

in the channel with $R = 4\,a_0$ compared to the case of $R_{\min} = 5\,a_0$. The reason is that the entropic barrier imposed by the constriction is higher than the one for $R_{\min} = 5\,a_0$, where already at equilibrium the polymer is more extended in axial direction. When comparing the deformation at $|x| = 9a_0$, evidently molecules have to squeeze more in radial direction when passing a constriction of $R_{\min} = 4\,a_0$, thus elongating in axial direction. Therefore, for the small narrowing all polymers show large values of the shape parameter when located at $|x| = 9\,a_0$, compare Figs. 7(a) [7(b),7(c)] to 7(d) [7(e),7(f)].

5   Knot conformations and modes of translocation

For both radii, we identified the Peclet number as the limiting factor for a successful topological separation. Interestingly, a constriction radius of $R_{\min} = 5\,a_0$ is slightly larger than the radius of gyration of the knotted portion of the 3_1 and 4_1 topologies, whereas $R_{\min} = 4\,a_0$ has approximately the same radius as the radius of gyration of the knotted subsection, when disregarding the repulsive wall potential. Figure 8 shows the knot gyration radius as a function of the CoM projected onto the longitudinal axis of a single chamber. The steric hindrance imposed by the $R_{\min} = 4\,a_0$ for translocation can be deduced by the data shown in Figs. 8(a) and 8(b). Comparison of Figs. 8(a)[8b)] to 8(c)[8(d)] reveals that for $R_{\min} = 5\,a_0$ the knot hardly changes size, whereas for the smaller narrowing, the knot has to shrink significantly to translocate; this shrinking represents an additional entropic barrier. Comparing the 4_1 knot to the 3_1 indicates that the more complex knot topology is slightly larger and shrinks less. As for the shape parameter, the average knot size gets more uniform with increasing flow strength, accelerating translocation.

As the narrower constriction imposes a strong confinement and high hindrance to the part containing the essential crossings, its compression represents a non-negligible, additional entropic penalty. Taking into account the results of nanopores, which can block the
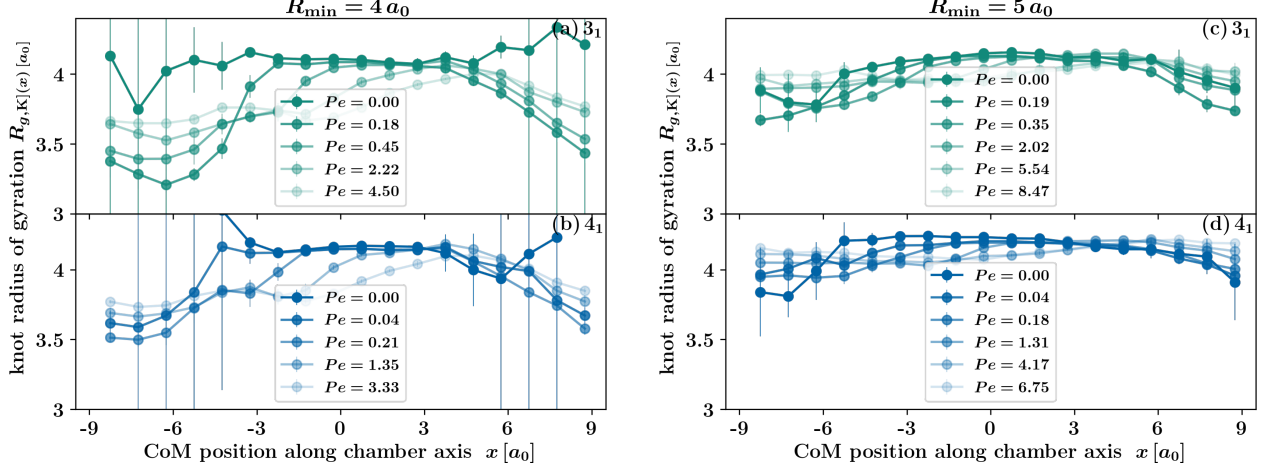
Figure 8: Radius of gyration of the knotted subsection $R_{g,K}$ along the CoM position along the chamber axis x for a narrowing of $R_{\min} = 4\,a_0$ ((a)-(b)) and $R_{\min} = 5\,a_0$ ((c)-(d)). The trefoil knot is depicted in green, the figure-of-eight knot in blue. With lightening color the flow strength increases.

translocation of the knotted portion when their radius, $R_{\min}$, is comparable to the size of a monomer,[40] it is surprising that a ratio of knot size to constriction radius smaller than unity is *not* a necessary condition for successful separation.

The severe restrictions imposed on the knots by $R_{\min} = 4\,a_0$ manifest themselves as well in the probability distribution of knot length, $P(\ell_K)$, shown in Figs. 9(a) and 9(b). At high flow strengths, when the knot passes more frequently through the narrowings, cf. Fig. 5, the ℓ_K distribution becomes broader but it also shifts towards smaller values, a combined consequence of confinement and tightening due to shear.[41] For the case $R_{\min} = 5\,a_0$, depicted in Fig. 9(c) and 9(d), we likewise observe a reduction of the average knot length when $Pe > 1$; however the wider constriction exerts less influence on knot size, whereas the effect due to shear is larger as polymers have higher Peclet numbers.

To investigate how the knotted region interacts with the constrictions, we examined the longitudinal positions of the KCoM and the CoM at various translocation stages. When CoM and KCoM are in the same chamber, denoted as $n_C = n_K$, the CoM can translocate into the adjacent chamber, described as $\curvearrowright C$, and, occasionally, subsequently pulls the KCoM into this chamber to complete in this way the translocation, the pulling event denoted as $K \to C$. Being it exclusively a two step process, the probability of its occurrence is computed from the
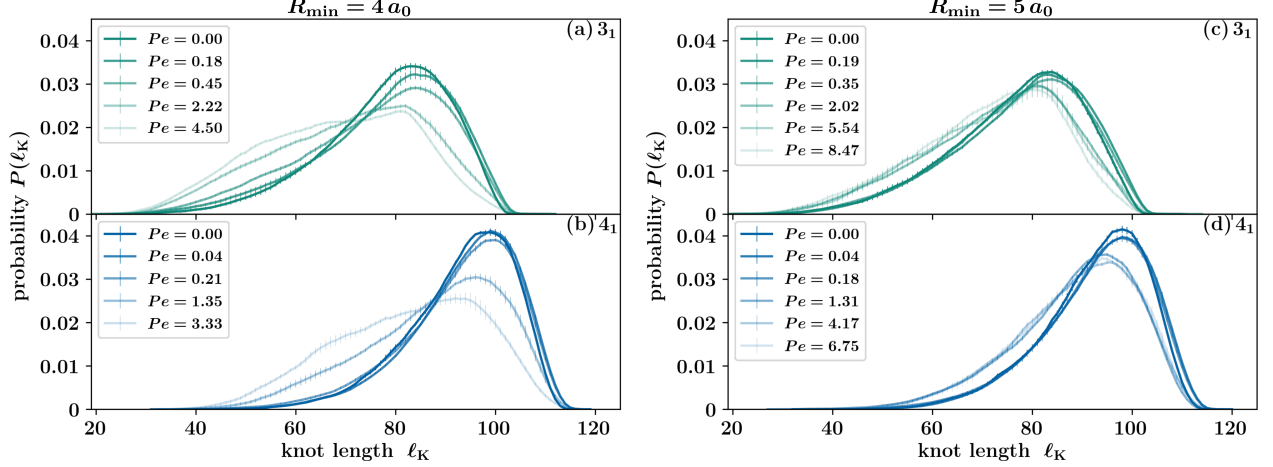
Figure 9: Probability distribution $P(\ell_K)$ of the knot length ℓ_K in a channel of narrowing $R = 4\,a_0$ in the case of a trefoil 3_1 (a) and 4_1 knot (b). The same quantity is depicted for a constriction radius $R_{\min} = 5\,a_0$ for the 3_1 (c) and 4_1 (d) knot. With lightening color the average fluid flow velocity increases.

composition of the probabilities of the two elementary events, $P(K \to C \cap \curvearrowright C \cap n_C = n_K)$. The relative importance of this CoM-led translocation event compared to the knot leading the crossing motion is given by the ratio μ:

$$\mu = \frac{P(K \to C \cap \curvearrowright C \cap n_C = n_K)}{P(C \to K \cap \curvearrowright K \cap n_C = n_K)} \ . \tag{9}$$

Clearly, $\mu > 1$, indicates a translocation dominantly initiated by CoM pulling KCoM behind. Conversely, if $\mu < 1$, KCoM translocates first. Here, we defined the probability of an event as the fraction of such events of the whole trajectory. Note that the probability can depend on the time interval with which trajectories are sampled. For a robust calculation of the probability we used a time interval of $0.1\,\tau$, where τ is the longest relaxation time of each topology, see Table 1.

Figure 10 shows the ratio, μ, as a function of flow strengths for the two constriction radii, revealing an opposite tendency only determined by $R_{\min}$. For $R_{\min} = 4\,a_0$ (solid lines), translocation is in the vast majority of cases led by CoM dragging KCoM behind at all flow strengths. For this constriction radius, the knot has to shrink to translocate and
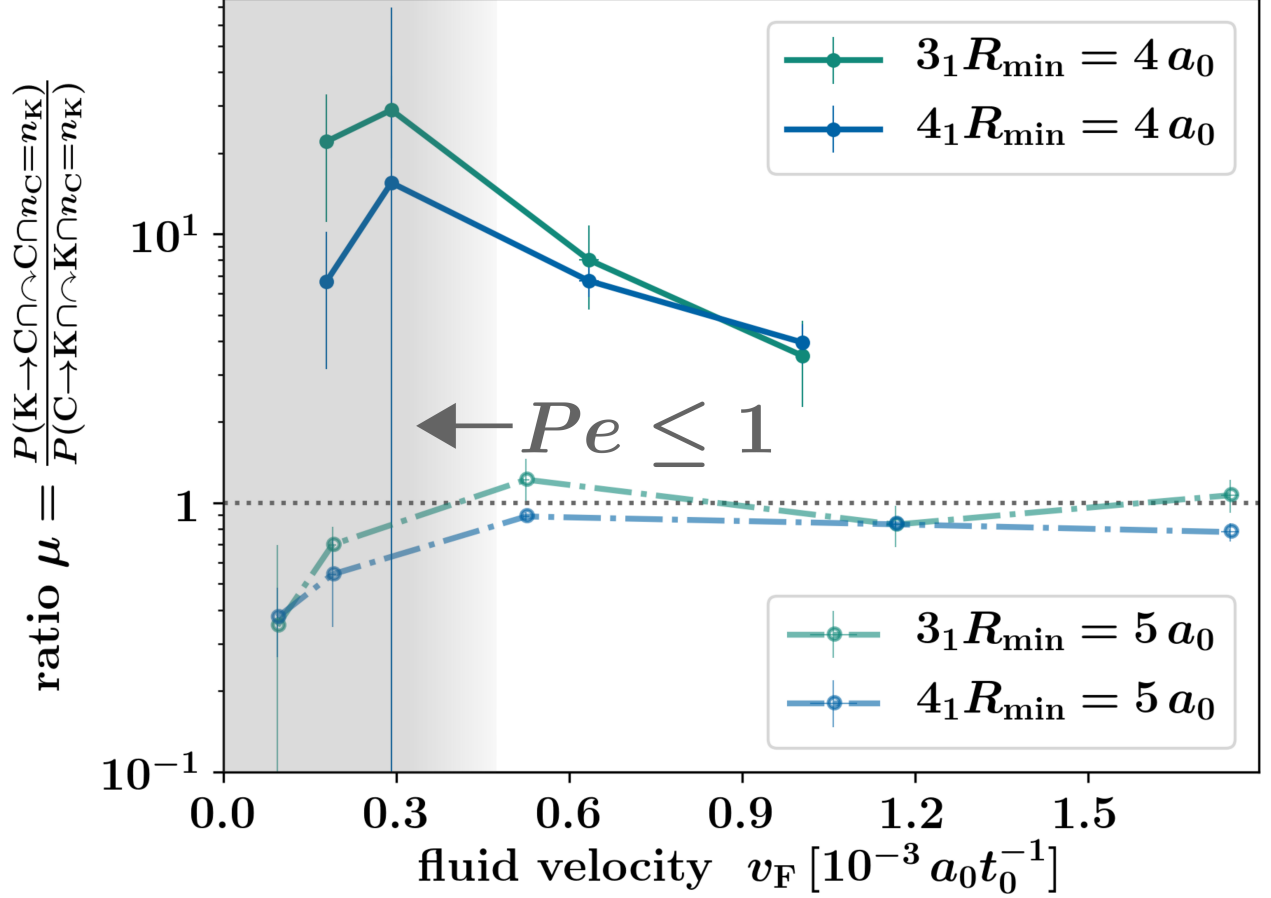
Figure 10: The ratio μ of the probability that translocation is led by CoM over it being led by KCoM. Solid lines show results for $R_{\min} = 4\,a_0$, dashed-dotted for $R_{\min} = 5\,a_0$.

it subsequently expands upon entering a new chamber, as shown in Figs. 8(a)-8(b). The behavior associated with the rare scenario of the knot leading translocation, is consistent with the effects of a backflow created by the effectively denser knotted region and acting on the trailing unknotted portion. This backflow, will in addition hinder a subsequent translocation of CoM,[41,42] thus reinforcing the incidence of the CoM-led process.

Surprisingly, a modest enlargement of the constriction to $R_{\min} = 5\,a_0$ completely changes the behavior of μ and hence the balance of the two translocation modes. Low flow strengths ($Pe \leq 1$) favor KCoM-led translocations, whereas for $Pe > 1$ there is no preference of KCoM- over CoM-led modes and $\mu \approx 1$. Here, the radius $R_{\min}$ is slightly larger than the average knot gyration radius, thus the essential crossings impose only a minor additional hindrance. Hence, the average knot size is rather constant across a chamber, see Figs. 8(c)-8(d), and

transport can occur without requiring excessive shrinking and expansion of the knot. For $Pe \leq 1$ translocation is initiated by a subpart of the polymer diffusing into an adjacent chamber. Since the knot represents a significant fraction of the whole polymer, this explains the dominance of a knot-led process. This mechanism breaks down at high flow strength, when motion is governed by convection, resulting in $\mu \approx 1$. The aforementioned backflow acts as well in the case of the larger constriction and explains the delay of knotted structures versus the unknot.
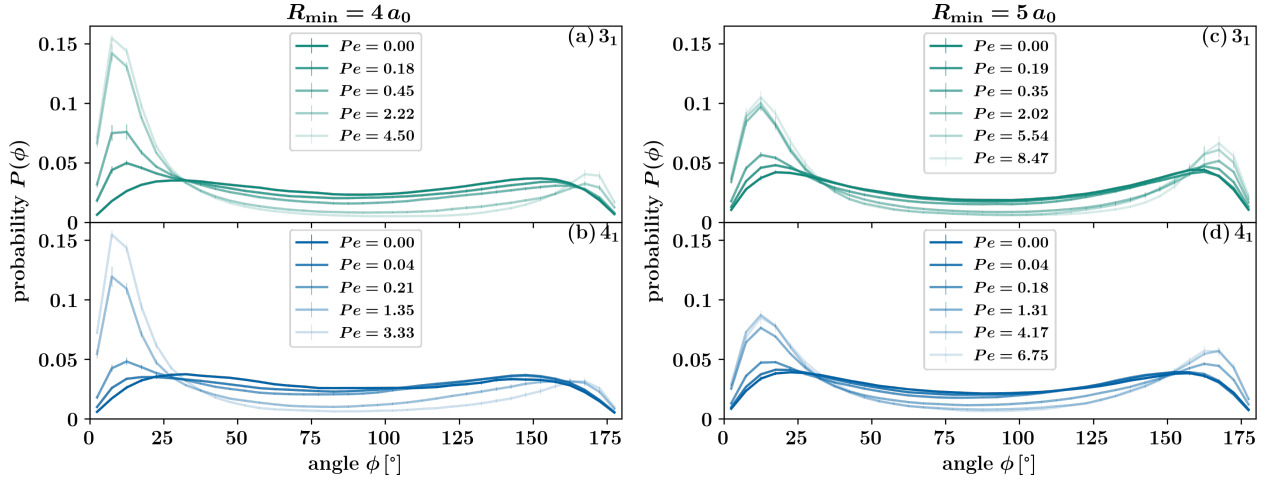

Figure 11: Normalized probability distribution $P(\phi)$ of the angle ϕ between the vector $w_{\mathrm{KCoM} \to \mathrm{CoM}}$ and flow direction. An angle of $\phi = 0$ corresponds to a an orientation where CoM is before KCoM with respect to flow direction. (a)-(b) are for a narrowing of $R_{\min} = 4\,a_0$, (c)-(d) for $R_{\min} = 5\,a_0$. With lightening color flow strength increases.

To investigate the translocation process in more detail, we examined the vector $\mathbf{w}_{\mathrm{KCoM} \to \mathrm{CoM}}$ pointing from KCoM to CoM. We looked at the probability distribution $P(\phi)$ of the angle ϕ subtended between flow direction and $\mathbf{w}_{\mathrm{KCoM} \to \mathrm{CoM}}$. This distribution is averaged over all possible positions along the channel axis. Thus, at low flow strength, when the knot rarely translocates it is dominated by configurations, when the polymer is close to the center of the chamber at $R(x) = R_{\max}$. In such a scenario, there is no preferred orientation. Thus the distribution of ϕ is rather uniform. At high flow strength, we see in Figs. 11(a)-11(b) for $R = 4\,a_0$ a strong preference for small angles, corresponding to a preferred orientation led by CoM, whereas in 11(c)-11(d) the distribution is bimodal with modes at $\phi \approx 0$ and

$\phi \approx 180°$. Please note that this distribution is based on all orientations of $\mathbf{w}_{\text{KCoM}\rightarrow\text{CoM}}$ in the whole simulation and not only the ones during a translocation process, which explains why Figs. 11(c) and 11(d) are not a symmetric bimodal distribution at high flow strengths.

6 Conclusion

We have examined the hydrodynamic transport of knotted ring polymers through nanochannels with a periodic hourglass topography. As a proof of concept we have focused in this work on the three simplest knot types, the unknot, trefoil and figure-of-eight knots. We established that the average transport velocities of different knot types can differ by up to an order of magnitude as long as flows with $Pe < 1$ are used. In this regime, transport can occur in two different modes, depending on whether the knotted or unknotted portion of the rings lead the motion through the constrictions. Remarkably, both modes allow for the efficient topological sorting of ring polymers. Increasing the flow velocity further, such that $Pe > 1$ for every topology, obliterates the topology-dependent component of the transport process, destroying any possibility of reliably separating a topological mixture. The loss of the topology-dependent response occurs when the convective flow is strong enough that polymers cannot relax and adjust to the local modulations of the channels. We hypothesize that differences in transport velocities will be observable for ring polymers with more complex topologies than considered here. As a part of future work, it will be particularly interesting to address systematically how these differences depend on the crossing number, a standard measure of complexity of knots, as well as their twist or torus character, which affects the translocation compliance through narrow pores[43] and the mean displacement of the knot in elongational flow fields.[44] The simplest way to address the latter point would be through a comparison of 5_1 and 5_2 knotted rings, which have same nominal complexity, but belong to the family of torus and twist knots, respectively. The results shed new light on the out-of-equilibrium response of entangled polymers in spatial confinement and we expect

them to be useful to inform the design of new types nanofluidics setups for the continuous topological sorting of polymers.

Acknowledgement

This document is the Accepted Manuscript version of a Published Work that appeared in final form in Macromolecules, copyright American Chemical Society after peer review and technical editing by the publisher. To access the final edited and published work see here.

References

(1) Amin, S.; Khorshid, A.; Zeng, L.; Zimny, P.; Reisner, W. A nanofluidic knot factory based on compression of single DNA in nanochannels. *Nat. Commun.* **2018**, *9*, 1506.

(2) Klotz, A. R.; Soh, B. W.; Doyle, P. S. Motion of Knots in DNA Stretched by Elongational Fields. *Phys. Rev. Lett.* **2018**, *120*, 188003.

(3) Soh, B. W.; Klotz, A. R.; Doyle, P. S. Untying of Complex Knots on Stretched Polymers in Elongational Fields. *Macromolecules* **2018**, *51*, 9562–9571.

(4) Micheletti, C.; Orlandini, E. Knotting and Unknotting Dynamics of DNA Strands in Nanochannels. *ACS Macro Lett.* **2014**, *3*, 876–880.

(5) Möbius, W.; Frey, E.; Gerland, U. Spontaneous Unknotting of a Polymer Confined in a Nanochannel. *Nano Lett.* **2008**, *8*, 4518–4522.

(6) Dai, L.; Renner, C. B.; Doyle, P. S. Metastable Knots in Confined Semiflexible Chains. *Macromolecules* **2015**, *48*, 2812–2818.

(7) Nakajima, C. H.; Sakaue, T. Localization and size distribution of a polymer knot confined in a channel. *Soft Matter* **2013**, *9*, 3140.

(8) Micheletti, C.; Orlandini, E. Knotting and metric scaling properties of DNA confined in nano-channels: a Monte Carlo study. *Soft Matter* **2012**, *8*, 10959.

(9) Reifenberger, J. G.; Dorfman, K. D.; Cao, H. Topological events in single molecules of *E.coli* DNA confined in nanochannels. *Analyst* **2015**, *140*, 4887–4894.

(10) Grosberg, A. Y.; Rabin, Y. Metastable Tight Knots in a Wormlike Polymer. *Phys. Rev. Lett.* **2007**, *99*, 217801.

(11) Marenda, M.; Orlandini, E.; Micheletti, C. Sorting ring polymers by knot type with modulated nanochannels. *Soft Matter* **2017**, *13*, 795–802.

(12) Weiss, L. B.; Nikoubashman, A.; Likos, C. N. Topology-Sensitive Microfluidic Filter for Polymers of Varying Stiffness. *ACS Macro Lett.* **2017**, *6*, 1426–1431.

(13) Mikkelsen, M. B.; Reisner, W.; Flyvbjerg, H.; Kristensen, A. Pressure-Driven DNA in Nanogroove Arrays: Complex Dynamics Leads to Length- and Topology-Dependent Separation. *Nano Lett.* **2011**, *11*, 1598–1602.

(14) Weeks, J. D.; Chandler, D.; Andersen, H. C. Role of Repulsive Forces in Determining the Equilibrium Structure of Simple Liquids. *J. Chem. Phys.* **1971**, *54*, 5237–5247.

(15) Bishop, M.; Kalos, M. H.; Frisch, H. L. Molecular dynamics of polymeric systems. *J. Chem. Phys.* **1979**, *70*, 1299–1304.

(16) Kremer, K.; Grest, G. S. Dynamics of entangled linear polymer melts: A moleculardynamics simulation. *J. Chem. Phys.* **1990**, *92*, 5057–5086.

(17) Rubinstein, M.; Colby, R. H. *Polymer Physics*, 1st ed.; Oxford University Press: Oxford, 2003.

(18) Tubiana, L.; Orlandini, E.; Micheletti, C. Probing the Entanglement and Locating Knots in Ring Polymers: A Comparative Study of Different Arc Closure Schemes. *Prog. Theor. Phys. Suppl.* **2011**, *191*, 192–204.

(19) Tubiana, L.; Orlandini, E.; Micheletti, C. Multiscale Entanglement in Ring Polymers under Spherical Confinement. *Phys. Rev. Lett.* **2011**, *107*, 188302.

(20) Tubiana, L.; Polles, G.; Orlandini, E.; Micheletti, C. KymoKnot: A web server and software package to identify and locate knots in trajectories of linear or circular polymers. *Eur. Phys. J. E* **2018**, *41*, 72.

(21) Bianco, V.; Malgaretti, P. Non-monotonous polymer translocation time across corrugated channels: comparison between Fick-Jacobs approximation and numerical simulations. *J. Chem. Phys.* **2016**, *145*, 114904.

(22) Han, J.; Craighead, H. G. Separation of Long DNA Molecules in a Microfabricated Entropic Trap Array. *Science* **2000**, *288*, 1026–1029.

(23) Malevanets, A.; Kapral, R. Continuous-velocity lattice-gas model for fluid flow. *Europhys. Lett.* **1998**, *44*, 552–558.

(24) Malevanets, A.; Kapral, R. Mesoscopic model for solvent dynamics. *J. Chem. Phys.* **1999**, *110*, 8605–8613.

(25) Padding, J. T.; Louis, A. A. Hydrodynamic interactions and Brownian forces in colloidal suspensions: Coarse-graining over time and length scales. *Phys. Rev. E* **2006**, *74*, 031402.

(26) Ihle, T.; Kroll, D. M. Stochastic rotation dynamics. II. Transport coefficients, numerics, and long-time tails. *Phys. Rev. E* **2003**, *67*, 066706.

(27) Ihle, T.; Kroll, D. M. Stochastic rotation dynamics. I. Formalism, Galilean invariance, and Green-Kubo relations. *Phys. Rev. E* **2003**, *67*, 066705.

(28) Kikuchi, N.; Pooley, C. M.; Ryder, J. F.; Yeomans, J. M. Transport coefficients of a mesoscopic fluid dynamics model. *J. Chem. Phys.* **2003**, *119*, 6388.

(29) Tüzel, E.; Strauss, M.; Ihle, T.; Kroll, D. M. Transport coefficients for stochastic rotation dynamics in three dimensions. *Phys. Rev. E* **2003**, *68*, 036701.

(30) Ihle, T.; Kroll, D. M. Stochastic rotation dynamics: A Galilean-invariant mesoscopic model for fluid flow. *Phys. Rev. E* **2001**, *63*, 020201(R).

(31) Ripoll, M.; Mussawisade, K.; Winkler, R. G.; Gompper, G. Dynamic regimes of fluids simulated by multiparticle-collision dynamics. *Phys. Rev. E* **2005**, *72*, 016701.

(32) Dahirel, V.; Zhao, X.; Couet, B.; Batôt, G.; Jardat, M. Hydrodynamic interactions between solutes in multiparticle collision dynamics. *Phys. Rev. E* **2018**, *98*, 53301.

(33) Malevanets, A.; Yeomans, J. M. Dynamics of short polymer chains in solution. *Europhys. Lett.* **2000**, *52*, 231–237.

(34) Götze, I. O.; Noguchi, H.; Gompper, G. Relevance of angular momentum conservation in mesoscale hydrodynamics simulations. *Phys. Rev. E* **2007**, *76*, 046705.

(35) Lamura, A.; Gompper, G.; Ihle, T.; Kroll, D. M. Multi-particle collision dynamics: Flow around a circular and a square cylinder. *Europhys. Lett.* **2001**, *56*, 319–325.

(36) Inoue, Y.; Chen, Y.; Ohashi, H. Development of a simulation model for solid objects suspended in a fluctuating fluid. *J. Stat. Phys.* **2002**, *107*, 85–100.

(37) Huang, C. C.; Chatterji, A.; Sutmann, G.; Gompper, G.; Winkler, R. G. Cell-level canonical sampling by velocity scaling for multiparticle collision dynamics simulations. *J. Comput. Phys.* **2010**, *229*, 168–177.

(38) Rouse Jr, P. E. A Theory of the Linear Viscoelastic Properties of Dilute Solutions of Coiling Polymers. *J. Chem. Phys.* **1953**, *21*, 1272.

(39) Zimm, B. H. Dynamics of polymer molecules in dilute solution: viscoelasticity, flow birefringence and dielectric loss. *J. Chem. Phys.* **1956**, *24*, 269–278.

(40) Suma, A.; Micheletti, C. Pore translocation of knotted DNA rings. *Proc. Natl. Acad. Sci. USA* **2017**, *114*, E2991–E2997.

(41) Liebetreu, M.; Ripoll, M.; Likos, C. N. Trefoil Knot Hydrodynamic Delocalization on Sheared Ring Polymers. *ACS Macro Lett.* **2018**, *7*, 447–452.

(42) Hsiao, K.-W. W.; Schroeder, C. M.; Sing, C. E. Ring Polymer Dynamics Are Governed by a Coupling between Architecture and Hydrodynamic Interactions. *Macromolecules* **2016**, *49*, 1961–1971.

(43) Suma, A.; Rosa, A.; Micheletti, C. Pore Translocation of Knotted Polymer Chains: How Friction Depends on Knot Complexity. *ACS Macro Lett.* **2015**, *4*, 1420–1424.

(44) Renner, C. B.; Doyle, P. S. Untying Knotted DNA with Elongational Flows. *ACS Macro Lett.* **2014**, *3*, 963–967.

Graphical TOC Entry